

See discussions, stats, and author profiles for this publication at: <https://www.researchgate.net/publication/231641350>

Chemical Dynamics Simulations of CO₂ Scattering off a Fluorinated Self-Assembled Monolayer Surface

ARTICLE *in* THE JOURNAL OF PHYSICAL CHEMISTRY C · NOVEMBER 2006

Impact Factor: 4.77 · DOI: 10.1021/jp064291v

CITATIONS

54

READS

21

3 AUTHORS, INCLUDING:



Emilio Martinez-Nuñez

University of Santiago de Compostela

86 PUBLICATIONS 1,020 CITATIONS

SEE PROFILE

Chemical Dynamics Simulations of CO₂ Scattering off a Fluorinated Self-Assembled Monolayer Surface

Emilio Martínez-Núñez,^{†,‡} Asif Rahaman,[†] and William L. Hase^{*,†}

Department of Chemistry and Biochemistry, Texas Tech University, Lubbock, Texas 79409, and Departamento de Química Física, Universidad de Santiago de Compostela, E-15706, Santiago de Compostela, Spain

Received: July 7, 2006; In Final Form: September 22, 2006

Chemical dynamics simulations at collision energies of 3.0, 10.6, and 20.0 kcal/mol were performed to study energy transfer in perpendicular ($\theta_i = 0^\circ$) collisions of carbon dioxide with a perfluorinated octanethiol self-assembled monolayer (F-SAM) surface. An accurate carbon dioxide + F-SAM intermolecular potential was developed from ab initio calculations extrapolated to the complete basis set limit. Three types of collision events are observed in the trajectories: direct scattering, physisorption on the top of the surface, and penetration of the surface. Energy transfer to carbon dioxide rotation and the final translational energy of carbon dioxide are both analyzed for each of these trajectory types. Penetration leads to near complete thermal accommodation with the F-SAM, whereas accommodation is not reached for either the direct or physisorption trajectories. The distributions of the translational energy and rotational angular momentum, $P(E_t)$ and $P(J)$, of the scattered CO₂ molecules and for the different trajectory types were analyzed to study their relationship to the atomic-level dynamics observed in the simulations. For each of the collision energies, these two distributions give similar thermal accommodation dynamics for the penetrating trajectories. For the physisorption trajectories, $P(E_t)$ and $P(J)$ are only similar at the lowest collision energy. These distributions are different at all collision energies for the direct trajectories, reflecting the complex dynamics for this trajectory type. The results found from these simulations are in excellent agreement with experiments for carbon dioxide scattering off perfluoropolyether (PFPE).

I. Introduction

Important fundamental information concerning gas–surface chemical dynamics may be obtained by studying energy transfer in collisions of gas-phase projectiles with surfaces.^{1–6} Organic surfaces are of particular interest, and recent work has focused on collisions of rare gas^{4,6–11} and oxygen^{5,12–17} atoms with these surfaces. Studies with rare gas atoms eliminate possible reactions and allow one to focus on the gas–surface energy transfer dynamics, which constitutes the initial elementary step in the adsorption of an inert particle into a liquid or solid.

Fundamental details of gas–surface energy transfer are more easily obtained if surfaces with well-ordered structures are used. Self-assembled monolayer (SAM) organic surfaces have this characteristic, are relatively straightforward to prepare, and have been used in a number of experimental studies. SAMs consisting of different hydrocarbon chains and different terminal groups may be studied.^{6,9,10,18–21} Of particular interest is the ability to identify and understand how changes in the surface structure and other surface properties affect the energy transfer dynamics. A range of surface attributes have been investigated, including the presence of hydrogen-bonding terminal groups (i.e., HO-SAM),^{6,18} interior hydrogen bonding,¹⁹ the role of the SAM packing density,⁹ and the effect of fluorination (i.e., H-SAM versus F-SAM).²¹ Each influences the energy transfer dynamics. Whether the number of C-atoms in the hydrocarbon chains of the SAM is odd or even also affects the energy transfer, since it determines the orientation of the SAM's terminal group.²⁰

Chemical dynamics simulations have played an important role in interpreting the energy transfer dynamics for rare gas atom collisions with SAMs.^{4,8–11,22–28} The simulation results agree with experiment, and they provide an atomic-level understanding of the gas–surface collision dynamics. They provide information regarding the relative importance and roles of physisorption on the surface interface, surface penetration, and direct inelastic scattering in the energy transfer. The systems investigated by the simulations are Ne + H-SAM/Au{111},^{4,22–27} Ar + H-SAM/Ag{111},^{9,10} Ar + H-SAM/Au{111},^{8–10,28} and Xe + H-SAM/Au{111}.¹¹

In atom collisions with a surface the only energy transfer pathway is that for transfer of the collision energy E_i to the surface vibrational degrees of freedom; i.e., an $E_i \rightarrow \Delta E_{\text{surf}}$ process. For a polyatomic projectile, E_i may also be transferred to the projectile's rotational and vibrational degrees of freedom, and it is of interest to understand how the energy transfer dynamics is influenced by these additional pathways. Furthermore, energy transfer to projectile vibration may be mode specific, and transfer to projectile rotation may depend on the moments of inertia for the rotational axes, which suggests additional possible delineations of the pathways for energy transfer. Recent experiments^{29,30} have probed the energy transfer dynamics in HCl collisions with H-SAM/Au{111} and HO-SAM/Au{111} surfaces and have been compared with the rare gas results.

In the work presented here chemical dynamics simulations were used to study CO₂ scattering off a model of the 1-perfluorinated octanethiol self-assembled monolayer (F-SAM) adsorbed on Au{111}. The simulations are performed at the same

* Corresponding author.

[†] Texas Tech University.

[‡] Universidad de Santiago de Compostela.

TABLE 1: Parameters Employed in the Potential Energy Surface of the System and Vibrational Frequencies of Carbon Dioxide

CO ₂ potential parameters			
k_r (mdyn/Å)	15.050	r_{eq} (Å)	1.170
k_b (mdyn Å/rad ²)	0.784	θ_{eq} (deg)	180.0
CO ₂ vibrational frequencies/(cm ⁻¹)			
model		experimental	
667 (2), 1 264, 2 419		667 (2), 1 333, 2 349	
interaction potential parameters ^a			
A_{CC}	5 681.4310867934	A_{CF}	53 851.8930562642
B_{CC}	2.7432340881	B_{CF}	3.9448913829
C_{CC}	-867 093.06384768	C_{CF}	-1 699.09764440
D_{CC}	14.6888366373	D_{CF}	7.5656310504
A_{OC}	23 188.6646353814	A_{OF}	73 460.2485602919
B_{OC}	3.2888988179	B_{OF}	4.1750200953
C_{OC}	-1 344.30298662	C_{OF}	-428.78936705
D_{OC}	6.1690402841	D_{OF}	6.6390027787

^a The units are such that the potential is in kcal/mol and distances in angstroms.

conditions as those for an experimental study of CO₂ scattering off perfluoropolyether (PFPE).³¹ The results of this study provide an atomic-level description of the energy transfer dynamics for CO₂ scattering off a fluorinated hydrocarbon surface and may be compared with the CO₂ + PFPE study. High-level ab initio calculations were employed to develop an accurate CO₂ + F-SAM intermolecular potential, and a published model was used for the F-SAM surface potential.³²

II. Computational Procedure

A. Potential Energy Surface. The total potential energy function for the system is written as

$$V = V_{CO_2} + V_{F-SAM} + V_{inter} \quad (1)$$

where V_{CO_2} is the potential for carbon dioxide, V_{F-SAM} is the potential for the fluorinated alkylthiolate self-assembled monolayer (F-SAM) surface, and V_{inter} is the interaction potential between CO₂ and the surface. The CO₂ potential consists of harmonic stretches and a harmonic bend and is expressed as

$$V_{CO_2} = \sum_{i=1}^2 0.5k_s(r_i - r_{eq})^2 + 0.5k_b(\theta - \theta_{eq})^2 \quad (2)$$

The parameters in eq 2 are collected in Table 1 and were optimized to fit the CO₂ experimental vibrational frequencies. Table 1 also lists the vibrational frequencies obtained with the CO₂ potential energy function, which are compared with the experimental values.³³ Agreement between the model potential vibrational frequencies and the experimental values is very good. In particular, the zero-point vibrational energy calculated with our potential is 2 508.5 cm⁻¹, which compares very well with the experimental value of 2 508 cm⁻¹.

The fluorinated alkylthiolate self-assembled monolayer (F-SAM) surface consists of 48 chains of the CF₃(CF₂)₇S radical absorbed on a single layer of 225 Au atoms. The chains are adsorbed in a shape of a rhombus, to correspond to experiment.³⁴ The S atom is absorbed on a hollow site of the Au{111} surface. The interaction between S and the Au atoms is modeled by harmonic stretch potentials between S and the three gold atoms comprising the hollow site, with a force constant of 2.8 mdyn Å⁻¹.³⁵ The gold atoms are used as a rigid anchoring slab held

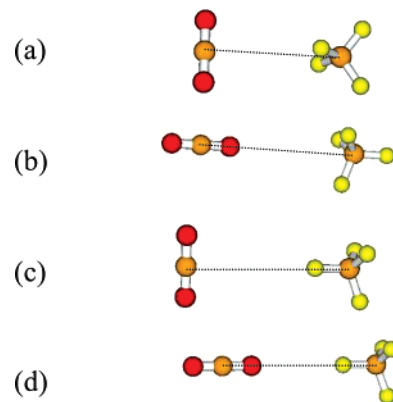


Figure 1. The CO₂...CF₄ orientations considered for the ab initio calculations.

at their equilibrium positions, and therefore their coordinates were not updated during the integration of the trajectories. Previous work has shown that projectile/SAM collision energy transfer dynamics is insensitive to whether the Au-surface is treated as rigid, a multilayer with vibrating atoms, or a thermal bath.²⁵ The potential energy function used for the F-SAM was developed in previous work.³² It consists of a sum of nonbonded interactions between the C₈F₁₇S chains and also includes stretching, bending, and dihedral terms for each chain

$$V_{F-SAM} = \sum_i \sum_j A \exp(-Br_{ij}) + \frac{C}{r_{ij}^D} + \sum_i 0.5k_s(r - r_{eq})^2 + \sum_i 0.5k_b(\theta - \theta_{eq})^2 + \sum_i 0.5k_t(1 - \cos(n\phi)) \quad (3)$$

The parameters for this potential are given in ref 32.

Experimental studies³⁴ show that the F-SAM monolayer forms a hexagonal close-packed structure with the nearest-neighbor direction rotated ~30° with respect to the Au{111} lattice and that the backbone of the CF₃(CF₂)₇S moiety has a small “tilt-angle” of ~12° with respect to the surface normal. A molecular dynamics simulation was performed of the F-SAM structure at 300 K, using the above potential energy model, and the values obtained for these two angles are 30.0° and 13.7°, respectively. The model potential energy surface used here gives a structure for the surface that is in excellent agreement with experiment.

Ab initio potentials were calculated for CO₂ + CF₄ to model V_{inter} for CO₂ interacting with the carbon and fluorine atoms of the F-SAM. Intermolecular curves, at the MP2/cc-pVXZ (with X = D,T,Q) level of theory,^{36,37} were calculated for the four CO₂ + CF₄ orientations depicted in Figure 1. These calculations were corrected for basis set superposition errors (BSSE), using the standard counterpoise method of Boys and Bernardi.³⁸ The calculations were also extrapolated to the infinite basis set limit according to the equation proposed by Peterson et al.³⁹

$$E(n) = E_{CBS} + A \exp[-(n + 1)] + B \exp[-(n + 1)^2] \quad (4)$$

where $n = 2, 3$, and 4 represent the DZ, TZ, and QZ energies, respectively.

Figure 2 shows the results of the MP2/cc-pVDZ, MP2/cc-pVTZ, MP2/cc-pVQZ, and MP2/CBS limit calculations for the four configurations in Figure 1, after BSSE corrections. The depths and positions of the intermolecular potential energy curves for these configurations are listed in Table 2. The CBS results were fit with the following analytic function, written as

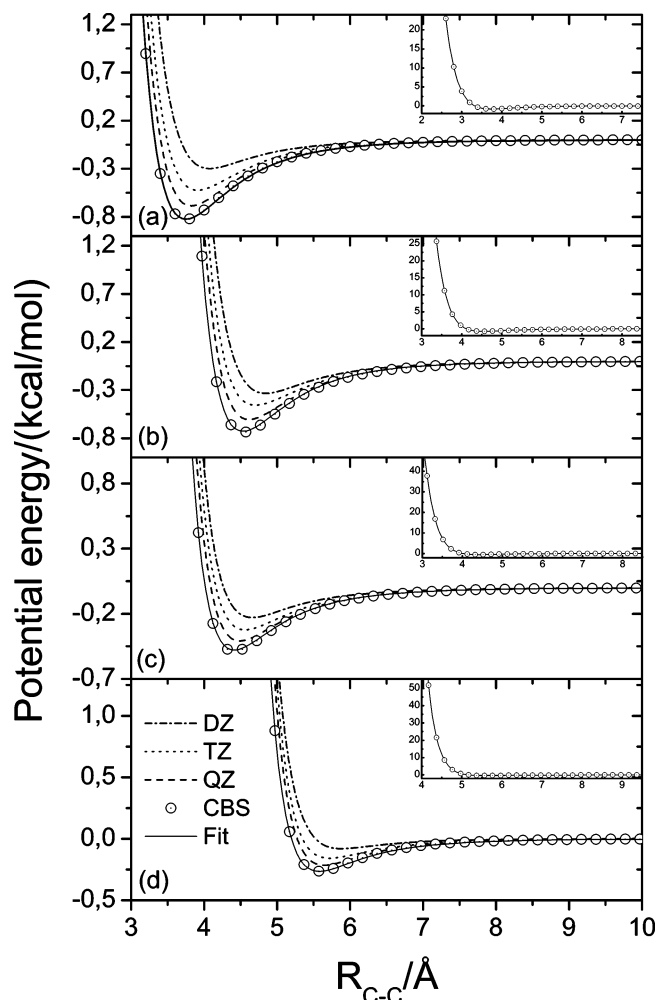


Figure 2. Ab initio calculations of and fits to the $\text{CO}_2 \cdots \text{CF}_4$ intermolecular potential for the configurations in Figure 1. The results of the MP2 calculations with the cc-pVXZ (X = D,T,Q) basis sets are given by spline fits. The ab initio points are shown for the CBS extrapolation. The curve through the CBS points is the fit described in section II.A. A BSSE correction was included in the ab initio calculations.

TABLE 2: Minima for $\text{CO}_2 \cdots \text{CF}_4$ Potential Energy Curves^a

curve ^b	cc-pVDZ		cc-pVTZ		cc-pVQZ		CBS	
	R_0	V_0	R_0	V_0	R_0	V_0	R_0	V_0
A	4.07	-0.30	3.91	-0.53	3.82	-0.68	3.76	-0.82
B	4.84	-0.33	4.70	-0.46	4.62	-0.61	4.55	-0.73
C	4.66	-0.23	4.56	-0.32	4.49	-0.41	4.41	-0.48
D	5.89	-0.08	5.71	-0.16	5.64	-0.21	5.57	-0.27

^a The position, R_0 , and depth, V_0 , are given for the minima of the potential energy curves in Figure 2. R_0 , the C-C distance is in Å, and V_0 is in kcal/mol. ^b The configurations for the curves are depicted in Figure 1.

a sum of two-body C-C, C-F, O-C, and O-F potentials for CO_2 interacting with the F-SAM

$$V_{\text{inter}} = \sum_i \sum_j A_{ij} \exp(-B_{ij} r_{ij}) + \frac{C_{ij}}{r_{ij}^{D_{ij}}} \quad (5)$$

where i is C or O of CO_2 and j is C or F of CF_4 . A nonlinear least-squares program was used for the fitting,⁴⁰ and the resulting parameters are collected in Table 1. The fit is shown in Figure 2. The root-mean-square error of the fitting is 5×10^{-2} kcal/mol.

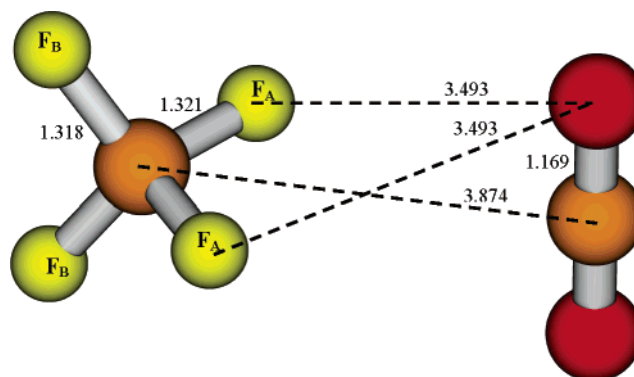


Figure 3. Structure of the $\text{CO}_2 \cdots \text{CF}_4$ van der Waals complex optimized at the MP2/cc-pVTZ level of theory. The structure of CO_2 undergoes very negligible change in forming the complex. The C-F bond length in isolated CF_4 is 1.3194 Å, intermediate to the C-F_A and C-F_B bond lengths. The FCF angles for the complex are $\text{F}_A\text{CF}_A = 109.25^\circ$, $\text{F}_B\text{-CF}_B = 109.62^\circ$, and $\text{F}_A\text{CF}_B = 109.49^\circ$.

Previous electronic structure calculations^{41,42} have investigated the structure and potential energy of the $\text{CO}_2 \cdots \text{CF}_4$ van der Waals complex, and it is of interest to compare with this work. Diep et al.⁴¹ performed MP2 calculations with the aug-cc-pVDZ and aug-cc-pVTZ basis sets. Explicit structural parameters were not given for the complex, but a depiction⁴¹ of the structure shows that CO_2 lies nearly parallel on an “edge” of CF_4 . With a BSSE correction included, these two basis sets give a binding energy of -0.58 and -0.79 kcal/mol, respectively. Fried and Hu⁴² performed MP2/6-311++G** calculations without a BSSE correction. The complex they found has a C-C separation of 3.84 Å, a binding energy of -1.44 kcal/mol, and a structure similar to that of Diep et al. Previous comparisons of van der Waals minima, determined with and without a BSSE correction,⁴³ indicate that the inclusion of a BSSE correction would decrease the depth of the well and move it to a longer C-C separation.

In comparison with the above studies, the structure of the $\text{CO}_2 \cdots \text{CF}_4$ complex was optimized at the MP2/cc-pVTZ level of theory with BSSE correction and is given in Figure 3. The initial structure was asymmetric and it optimized to a structure with C_{2v} symmetry within four significant figures for all intermolecular distances. Its structure is similar to those reported previously^{41,42} and has a C-C separation of 3.87 Å. There are negligible changes in the CO_2 geometry in forming the complex; however, there were small changes in the CF_4 geometry. Single point potential energies were then calculated at this structure, with BSSE correction, using MP2 theory with the cc-pVDZ, cc-pVTZ, and cc-pVQZ basis sets to extrapolate to the CBS limit (see eq 4). A similar set of calculations were performed using CCSD(T) theory except that the CCSD(T)/cc-pVQZ binding energy was approximated as the MP2/aug-cc-pVQZ energy plus the difference between the CCSD(T) and MP2 energies with the cc-pVTZ basis, i.e., the focal-point approximation.^{44,45} The resulting cc-pVDZ, cc-pVTZ, cc-pVQZ, and CBS binding energies are -0.19, -0.56, -0.74, and -0.86 kcal/mol using MP2 theory and are -0.20, -0.57, -0.76, and -0.87 kcal/mol using CCSD(T) theory. The MP2 and CCSD(T) energies are nearly the same, with the cc-pVQZ and CBS energies within 0.1 kcal/mol.

The structure of the van der Waals complex predicted by the fitted intermolecular potential, eq 5, was also determined. The CO_2 and CF_4 structures were also optimized as part of this calculation. The potential in Table 1 was used for CO_2 , and a model harmonic potential was used for CF_4 . The equilibrium

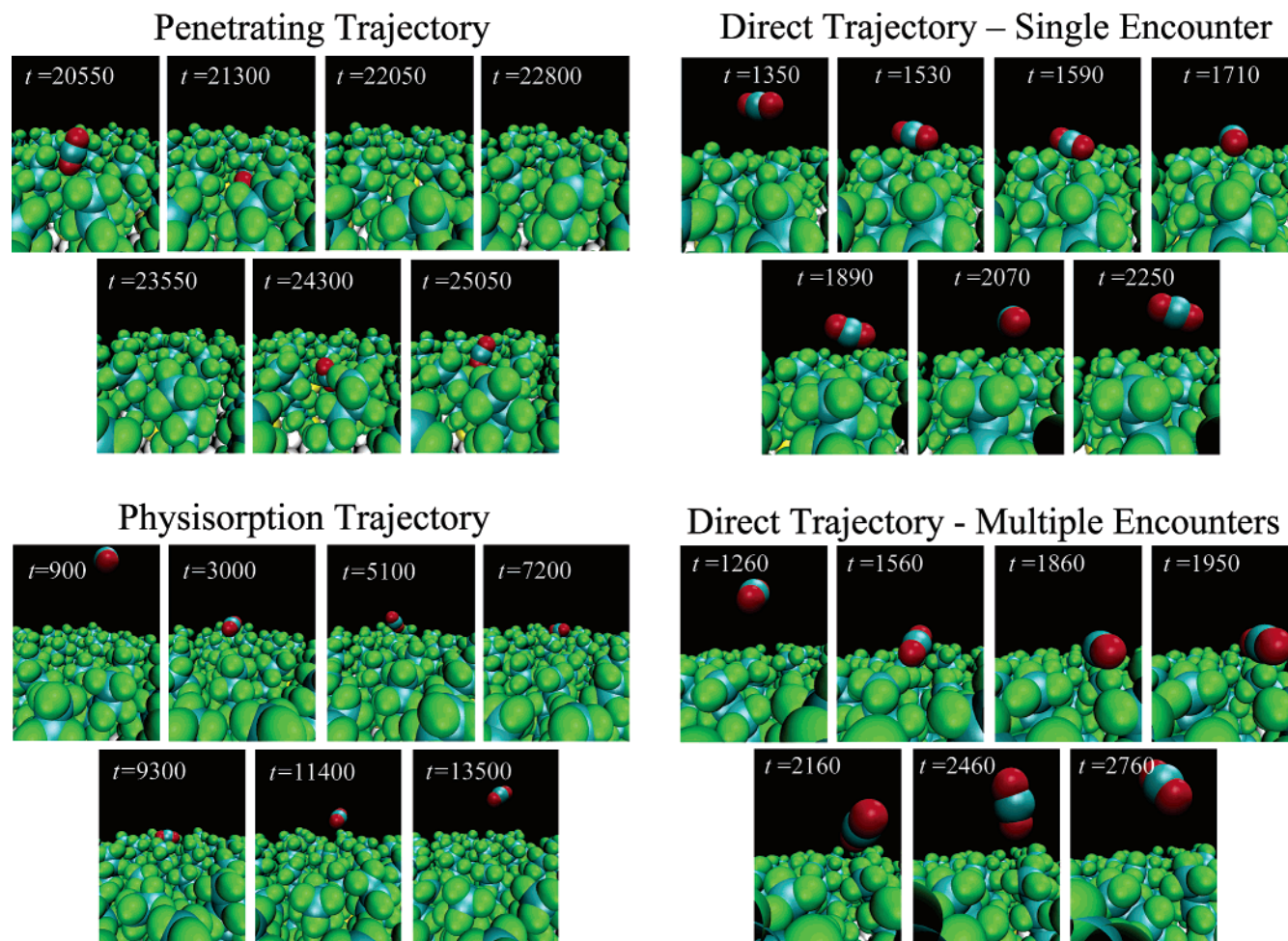


Figure 4. Snapshots, from representative trajectories, of direct, penetrating, and physisorption events.

angles for the latter were tetrahedral, and the MP2/cc-pVTZ value was 1.3194 Å for the C–F equilibrium distance. The force constants used for CF₄, $f_{\text{CF}} = 4.868 \text{ mdyn Å}^{-1}$ and $f_{\text{FCF}} = 1.666 \text{ mdyn Å/rad}^2$, are the values for the F-SAM.³² The resulting optimized structure and potential energy for the CO₂⋯CF₄ van der Waals complex are nearly the same as those for the MP2/cc-pVTZ optimized structure shown in Figure 3. For the analytic potential's complex, the C–C separation is 3.75 Å and binding energy is −0.82 kcal/mol.

B. Chemical Dynamics Calculations. The chemical dynamics calculations were performed using the VENUS05 computer program.⁴⁶ Initial conditions for the simulations mimic those employed in the experiments.³¹ Quasi-classical sampling⁴⁷ was used for CO₂ to add zero point energy to its vibrational normal modes and to add a temperature of 15 K to its rotational degrees of freedom. The incident angle (the angle with respect to the surface normal) for the CO₂ projectile was zero degrees, and collision energies E_i of 3.0, 10.6, and 20.0 kcal/mol were studied. The 10.6 kcal/mol energy was investigated experimentally.³¹ The carbon dioxide center-of-mass was randomly aimed at a point in the central unit cell of the surface, which is defined by the Cartesian coordinates of the terminal carbon atoms for three chains at the corner of the unit cell. The unit cell is defined by the vectors \vec{u} and \vec{v} , calculated from the Cartesian coordinates of these three carbon atoms, and the aiming point (\vec{A}) in the unit cell is determined randomly by

$$\vec{A} = R_1 \vec{u} + R_2 \vec{v} \quad (6)$$

where R_1 and R_2 are two freshly generated random numbers.

Periodic boundary conditions and the image vector convention⁴⁸ were employed to represent a larger surface. This was important, since some collisions resulted in physisorption and multiple CO₂ encounters with the surface.

The trajectories were initiated at a distance of 25 Å between the CO₂ center of mass and the surface aiming point, which places CO₂ at about 38 Å above the gold atoms. Ensembles of 2 112, 2 095, and 2 050 trajectories were integrated with a fixed step size of 0.3 fs using the Adams-Moulton algorithm in VENUS05 for E_i values of 3.0, 10.6, and 20.0 kcal/mol, respectively. Before the trajectory simulation began, the surface was relaxed to a thermodynamic equilibrium structure by a 2 ps molecular dynamics simulation⁴⁸ in which the atomic velocities are scaled during the integration to obtain a surface temperature of 300 K. This structure was then used as the initial structure of a 100 fs equilibration run at the beginning of each trajectory. When the trajectory is finished, the final translational, vibrational, and rotational energy of CO₂ and the final internal energy of the surface were calculated from the atomic Cartesian coordinates and momenta. The CO₂ rotational quantum number was also determined from the CO₂ rotational angular momentum. The trajectories were animated and visualized⁴⁹ to obtain an atomic-level description of the projectile–surface collisions. The maximum integration time for a trajectory was 150 ps.

III. Results

A. Trajectory Types and Residence Times. Three different types of trajectories were observed in the simulations. *Direct* collisions have only one inner turning point (ITP) in their motion

TABLE 3: Percentages of Different Trajectory Types

E_i^a	trajectory types ^b		
	direct	penetrate	physisorb
3.0	17	38 (0.2)	45
10.6	34	24 (1.1)	42
20.0	39	25 (3.5)	36

^a Collision energy in kcal/mol. ^b The trajectory types are described in the text. The percentages of the trajectories that penetrate with only one inner turning point are given in parentheses. The Au(s)–CO₂ interaction is not represented in the potential energy function, and 67, 61, and 51 trajectories at 3.0, 10.6, and 20.0 kcal/mol, respectively, for which CO₂ reached the Au surface, are not included in the analysis. The total trajectories calculated at these respective energies are 2112, 2095, and 2050.

TABLE 4: Average Residence Times^a

E_i^b	penetrate	physisorb
3.0	39.2	12.5
10.6	35.1	9.6
20.0	30.2	8.5

^a The residence time is in ps. ^b E_i is in kcal/mol.

perpendicular to the surface plane. These trajectories are often characterized as inelastic scattering (IS) events.^{50,51} There are two types of nondirect trajectory which are often grouped together as trapping desorption (TD).⁵¹ One is *physisorption*, in which CO₂ adsorbs for quite a long time on the surface. In this case, the trajectory undergoes several ITPs, and CO₂ remains adsorbed for several picoseconds. For the other nondirect trajectories, CO₂ *penetrates* the F-SAM. Penetration is identified by at least one of the atoms of CO₂ attaining a height above the Au surface of less than 11.6 Å, which is the height intermediate of the average 300 K heights of the C atoms of the –CF₃ terminal groups (12.2 Å) and of their adjacent –CF₂ groups (11.0 Å). Snapshots of four representative trajectories, illustrating these direct, physisorption, and penetration events, are shown in Figure 4. Two direct trajectories are shown. For one, CO₂ collides impulsively with only one alkylthiol chain. For the other, CO₂ has encounters with multiple chains.

Table 3 lists the percentages of the three trajectory types as a function of E_i . Physisorption decreases with an increase in E_i , while direct scattering increases. The penetration probability is relatively insensitive to the collision energy. A small number of the trajectories penetrate deep into the F-SAM and reach the Au surface. An accurate CO₂...Au(s) potential was not included in the simulations, and these trajectories were removed from the analyses. Their percentages are small and equal 3.2, 2.9, and 2.5 at E_i of 3.0, 10.6, and 20.0 kcal/mol, respectively.

A phenomenological residence time τ was determined for each trajectory by identifying it as the difference in the times of the last and first ITPs in the perpendicular motion of the CO₂ center-of-mass. For this model, a direct trajectory does not have a residence time. In other work,^{22,27} the residence time has been based on the time the projectile spends within a specified height above the surface, resulting in short residence times for direct trajectories. The average residence times determined by the ITP approach, for the penetrating and physisorption trajectories, are listed in Table 4.

The residence times decrease with an increase in E_i , with those for the penetration events somewhat larger than those for physisorption. Representative distributions of the penetration and physisorption residence times are shown in Figure 5. The distribution for the penetrating trajectories is peaked at $\tau > 0$ for E_i of 3.0 and 10.6 kcal/mol. However, for $E_i = 20.0$ kcal/mol, the distribution peaks at $\tau = 0$. Each of the penetrating

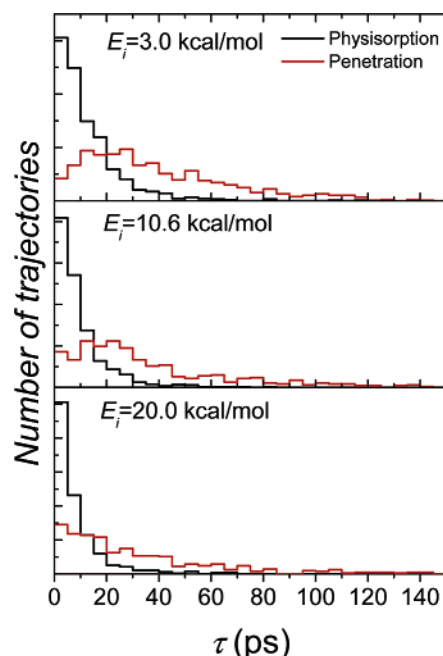


Figure 5. Representative distributions of residence times for penetrating and physisorbing trajectories. Results are for $E_i = 10.6$ kcal/mol. The red and black curves are for penetration and physisorption, respectively.

TABLE 5: Average Energies Transferred^a

	total	direct	penetrate	physisorb
$E_i = 3.0$				
$\langle \Delta E_{\text{int}} \rangle$	0.6 (19)	0.7 (23)	0.5 (15)	0.6 (20)
$\langle \Delta E_{\text{vib}} \rangle$	−0.3	−0.2	−0.5	−0.3
$\langle \Delta E_{\text{rot}} \rangle$	0.9	0.9	1.0	0.9
$\langle \Delta E_{\text{surf}} \rangle$	1.0 (34)	0.5 (16)	1.3 (45)	1.0 (32)
$\langle E_f \rangle$	1.4 (47)	1.8 (61)	1.2 (40)	1.4 (48)
$E_i = 10.6$				
$\langle \Delta E_{\text{int}} \rangle$	0.9 (9)	1.2 (11)	0.5 (5)	1.0 (9)
$\langle \Delta E_{\text{vib}} \rangle$	−0.3	−0.2	−0.5	−0.2
$\langle \Delta E_{\text{rot}} \rangle$	1.2	1.4	1.0	1.2
$\langle \Delta E_{\text{surf}} \rangle$	7.2(67)	6.0(57)	8.9(84)	7.0(66)
$\langle E_f \rangle$	2.5(24)	3.4(32)	1.2(11)	2.6(25)
$E_i = 20.0$				
$\langle \Delta E_{\text{int}} \rangle$	1.4(7)	1.8(9)	0.6(3)	1.5(7)
$\langle \Delta E_{\text{vib}} \rangle$	−0.3	−0.2	−0.4	−0.3
$\langle \Delta E_{\text{rot}} \rangle$	1.7	2.0	1.0	1.8
$\langle \Delta E_{\text{surf}} \rangle$	14.7(73)	13.1(66)	17.7(89)	14.2(71)
$\langle E_f \rangle$	3.9(20)	5.1(25)	1.7(8)	4.3(22)

^a Energy is in kcal/mol. The numbers in parentheses are the percent energy transfers.

trajectory residence time distributions has a long time tail extending to more than 100 ps. The physisorption residence time distributions peak at $\tau = 0$ and decrease exponentially with an increase in τ .

B. Energy Transfer Efficiencies and Distributions. During the collision some of the carbon dioxide incident energy E_i is transferred to the surface vibrations, E_{surf} , and CO₂ internal energy, E_{int} , with the remainder staying in CO₂ translational energy E_f

$$E_i = E_f + \Delta E_{\text{int}} + \Delta E_{\text{surf}} \quad (7)$$

The values of ΔE_{surf} , ΔE_{int} , and E_f are presented in Table 5. Most of the incident energy goes to the surface's vibrational modes, with the transfer to the surface increasing from 34 to 73 % as E_i is increased from 3.0 to 20.0 kcal/mol. Concomitantly, the percent energy remaining in CO₂ translation de-

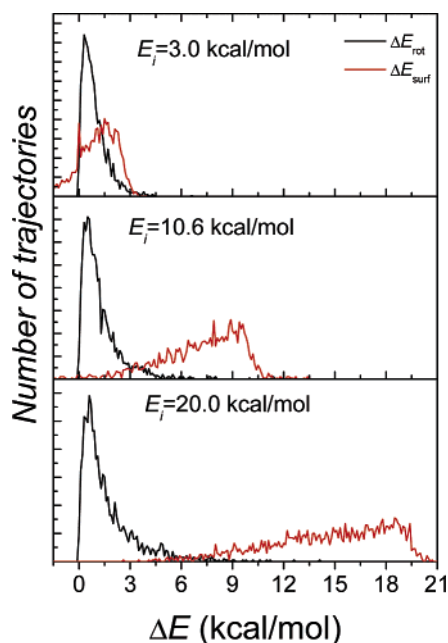


Figure 6. Distributions of ΔE_{surf} and ΔE_{rot} , CO₂ rotational energy. ΔE_{rot} and ΔE_{surf} are black and red curves, respectively.

creases. The percentage energy transfer to CO₂ internal energy is less dependent on E_i . Carbon dioxide's vibrational modes are not excited, and in fact, there is a slight decrease of -0.3 kcal/mol in its vibrational energy. As discussed below, this results from a change in the CO₂ bend vibrational angular momentum.^{52,53} The gain in the CO₂ internal energy results from an increase in its rotational energy.

Table 5 also includes the dependence of the energy transfer percentages on the trajectory type, i.e., direct, penetrating, or physisorbing. Overall, the results for the direct and physisorption trajectories are similar, with the former transferring somewhat less energy to ΔE_{surf} and more energy to E_f . The energy transfer pattern is different for the penetrating trajectories. A very large fraction of the collision energy is transferred to the surface, with a quite small fraction remaining in translation. With penetration, the amount of energy transferred to CO₂ rotation is approximately smaller by a factor of 2 than that amount found for both the direct and physisorption trajectories at the highest collision energy. Ten to twenty percent more energy is transferred to CO₂ rotation for the direct as compared to the physisorption trajectories.

The energy transfer distributions to ΔE_{surf} and to CO₂ rotation, ΔE_{rot} , for all the trajectories at each E_i , are shown in Figure 6. These distributions illustrate the overall efficient energy transfer to the surface, with less energy transfer to CO₂ rotation. However, there are events which transfer appreciable energy to CO₂ rotation and little to the surface. The distributions of the final CO₂ translation, $P(E_f)$, for all of the trajectories and for each of the three trajectory types are plotted in Figure 7. Each trajectory $P(E_f)$ distribution was fit using the method of Legendre moments as described previously.⁵⁴ (Histograms of $P(E_f)$ and the fits are compared in Figure 8. The distribution of the CO₂ rotational quantum J was also determined versus trajectory type, and this analysis is discussed in the next section). The $P(E_f)$ distributions for the direct trajectories are quite broad with a single peak. For the penetrating and physisorbing trajectories, the distributions appear bimodal, with a well-defined peak at small E_f . This peak is quite pronounced for the penetrating distribution, indicating efficient accommodation of E_f .

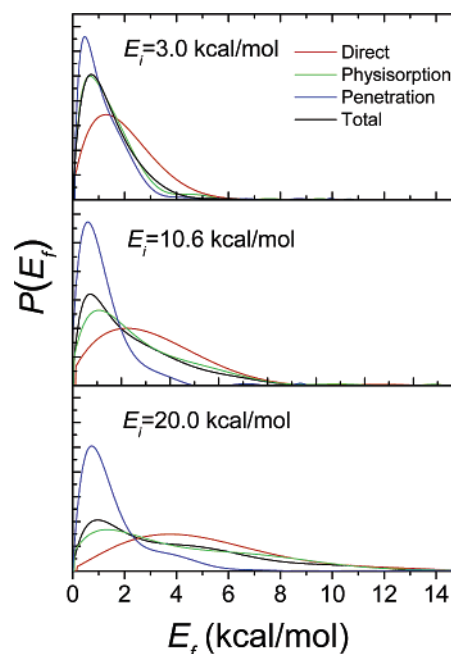


Figure 7. Distributions of the final CO₂ translational energy, E_f . Total trajectories (black curve), direct trajectories (red curve), penetrating trajectories (blue curve), and physisorption trajectories (green curve).

In previous studies of projectile scattering off hydrocarbon surfaces,^{4,23,50,51} the low-energy region of the $P(E_f)$ distribution has been fit to the Maxwell–Boltzmann distribution for thermal desorption⁵⁵

$$P(E_f) = (k_B T_s)^{-2} E_f \exp(-E_f/k_B T_s) \quad (8)$$

where T_s is the surface temperature. This type of analysis was performed here with T_s treated as the variable T_{BC} , as done in previous work.²³ The fits to the total $P(E_f)$ and to the individual $P(E_f)$ for the penetrating and physisorbing trajectories are shown in Figure 8, for the simulations with $E_i = 10.6$ kcal/mol. (There is not a Boltzmann component in the direct scattering trajectories.) The parameters for these fits and for those of the simulations at E_i of 3.0 and 20.0 kcal/mol are summarized in Table 6.

For both the total and physisorbing trajectories, the Boltzmann component in $P(E_f)$ decreases and its temperature increases with increase in E_i . This suggests an increased difficulty in thermal accommodation as the incident energy is increased. There is only a small decrease in the Boltzmann component from unity as E_i is increased to 20.0 kcal for the penetrating trajectories. There is complete thermal accommodation of the Boltzmann component at the two lowest E_i and near accommodation at the highest E_i .

Temperatures for Boltzmann components in $P(E_f)$ distributions, higher than the surface temperature, have been found in previous studies.²³ Such a result suggests that there is sufficient relaxation to form a Boltzmann distribution with a subset of the surface modes but insufficient accommodation for the scattered projectile to attain the surface temperature.²⁶

C. CO₂ Rotational Quantum Number Distribution $P(J)$. The rotational quantum number J , of the scattered CO₂ molecule, was determined from its rotational angular momentum j using the relationship

$$j = \sqrt{J(J+1)}\hbar \quad (9)$$

The distributions of $P(J)$ for the total trajectories, and the three

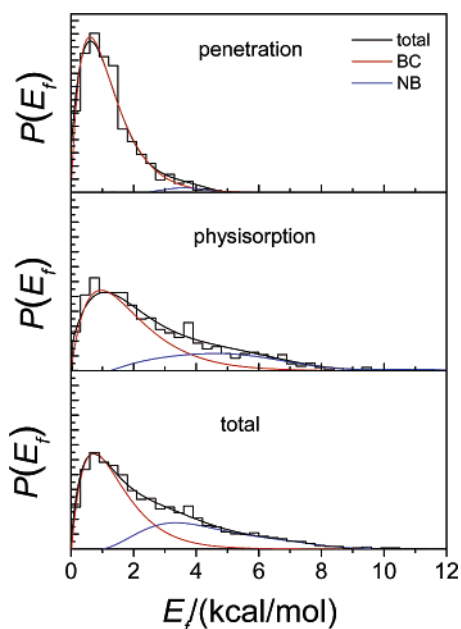


Figure 8. Boltzmann (BC) and non-Boltzmann (NB) components in the $P(E_i)$ distributions for the total, penetrating, and physisorbing trajectories at $E_i = 10.6$ kcal/mol. BC is indicated by a red curve and NB by a blue curve. The histogram is the total trajectory distribution, and the black curve is its fit by the method of Legendre moments.⁵⁴

TABLE 6: Parameters for the Boltzmann Fits to the $P(E_i)$ Distributions^a

E_i	total ^b	penetrate	physisorb
3.0	1.00, 365	1.00, 289	1.00, 364
10.6	0.63, 360	0.97, 304	0.71, 483
20.0	0.56, 491	0.91, 340	0.59, 617

^a The first number in each pair is the fraction of the Boltzmann component in the fit to $P(E_i)$, and the second is the temperature (K) for the Boltzmann component. ^b There is not a Boltzmann component in the direct scattering trajectories.

trajectory types, are given in Figure 9 for the simulations at $E_i = 10.6$ kcal/mol. In fitting the distributions, it was discovered that each contains low- and high-temperature Boltzmann components. The fraction of each component and its temperature are given in Table 7 for the $E_i = 10.6$ kcal/mol simulations, as well as those at 3.0 and 20.0 kcal/mol. In the determination of these fits, both the low and high temperatures were allowed to vary without restrictions. There is some uncertainty concerning the meaning of a low temperature less than 300 K for the total and penetrating trajectories, and additional fits were performed for these trajectory types at $E_i = 300$ K with the low temperature fixed at 300 K.

For each E_i , the fraction of the high-temperature component is largest for the direct trajectories and smallest for the penetrating trajectories. For the direct trajectories, the fraction of the low T component is quite small for E_i of 3.0 and 20.0 kcal/mol, and the distribution is well-approximated by a single Boltzmann distribution, which is particularly the case for E_i of 20.0 kcal/mol. For E_i of 3.0 kcal/mol the temperature of this single Boltzmann is close to the surface temperature of 300 K, whereas it is significantly higher for $E_i = 20.0$ kcal/mol. The $P(J)$ distribution for the penetrating trajectories is a single Boltzmann, with a temperature well-approximated by the surface temperature, for E_i of 3.0 and 10.6 kcal/mol. For $E_i = 20.0$ kcal/mol, the unconstrained fit to $P(J)$ for the penetrating trajectories is bimodal with a low temperature significantly lower than that of the surface temperature. Such a result may be

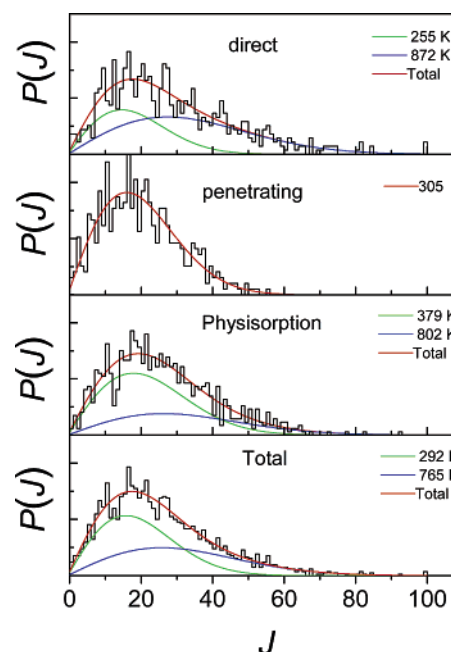


Figure 9. Distributions of the CO₂ rotational quantum number for the direct, penetrating, physisorption, and total trajectories. The fits were made with a sum of two Boltzmann distributions, and their temperatures are given. The fraction of each Boltzmann component is listed in Table 7.

TABLE 7: Parameters for the Boltzmann Fits to the $P(J)$ Distributions

E_i	low T^a		high T^a	
	frac.	T	frac.	T
total trajectories				
3.0	1.00	302		
10.6	0.58	292	0.42	765
20.0	0.34	242	0.66	948
	0.44	300 ^b	0.56	1 090
direct trajectories				
3.0	0.16	81	0.84	411
10.6	0.39	255	0.61	872
20.0	0.04	132	0.96	910
penetrating trajectories				
3.0	1.00	295		
10.6	1.00	305		
20.0	0.69	210	0.31	723
	0.94	300 ^b	0.06	2 832
physisorption trajectories				
3.0	1.00	304		
10.6	0.67	379	0.33	802
20.0	0.50	357	0.50	1 300

^a Fractions and temperatures for the two component Boltzmann fits to the $P(J)$ distributions. ^b The low temperature was fixed at 300 K in the fit.

physically unrealistic. Constraining the low-temperature component at 300 K gives a somewhat less accurate fit, with a small high-temperature fraction at 2 832 K. The suggestion is that thermal accommodation also occurs at $E_i = 20$ kcal/mol for the penetrating trajectories, as found for the lower E_i . This agrees with the finding that the average energy transferred to CO₂ rotation is the same for all the E_i (see Table 5).

It is possible that a more accurate representation of $P(J)$ for the penetrating trajectories at $E_i = 20$ kcal/mol can be obtained by the fit of a 300 K Boltzmann distribution to the low J

component and by simply calling the remainder of the distribution non-Boltzmann and not attempting to fit it to a second Boltzmann distribution. To discover whether this is more appropriate than the fit by a sum of two Boltzmann distributions will require calculating substantially more trajectories and obtaining a more accurate $P(J)$.

For the physisorption trajectories $P(J)$ is a single Boltzmann, at the surface temperature, for $E_i = 3.0$ kcal/mol. For the higher E_i , the physisorption $P(J)$ becomes bimodal with an average temperature significantly higher than that of the surface.

The following summarizes the $P(J)$ distributions for the trajectory types: (1) at $E_i = 3.0$ kcal/mol, $P(J)$ is well-approximated by a single Boltzmann with the surface temperature for each trajectory type; (2) there is ~ 300 K thermal accommodation of CO₂ rotation for the penetrating trajectories at each E_i ; and (3) for the physisorption trajectories, $P(J)$ is only a single Boltzmann distribution for the lowest E_i , and the average temperature of $P(J)$ increases with E_i . For E_i of 3.0, 10.6, and 20.0 kcal/mol, the $P(J)$ for the different trajectory types combine to respectively give a total $P(J)$ which is a single ~ 300 K Boltzmann distribution, a bimodal distribution with a low temperature component approximately equal to 300 K, and a bimodal distribution with a low-temperature component which may be 300 K.

D. Vibrational Angular Momentum. It should be noted that, in equating the rotational angular momentum quantum number to the total CO₂ rotational angular momentum in eq 9, no account is made for vibrational angular momentum.^{52,53} In the trajectory initial conditions, the CO₂ zero-point energy level is selected with all of the bend energy in vibration and none in rotation. However, the collision of CO₂ with the surface may transfer some of the collision energy to vibrational angular momentum and/or change the phase of the bend modes to introduce vibrational angular momentum into the bend energy. An analysis of the trajectories shows that the vibrational angular momenta of the scattered CO₂ molecules is quite small and that for $E_i = 10.6$ kcal/mol its average value is only $0.275 \hbar$. Such a small correction lies within the statistical uncertainty of the $P(J)$ distribution.

No attempt was made to determine the relative importance of collision energy transfer or of the change in the phase of the bend modes as the mechanism for CO₂ acquiring vibrational angular momentum. However, for the collisions at $E_i = 3.0$ kcal/mol the average rotational energy about the symmetry axis of the scattered CO₂ molecules is 0.28 kcal/mol. As shown in Table 5, this is approximately the decrease in the CO₂ vibrational energy, which suggests the gas-surface collision changes the phase of the CO₂ bends through bend-vibration to bend-rotation energy transfer. This is supported by comparing the CO₂ total rotational energy with RT . As discussed above and shown in Table 7, for the $E_i = 3.0$ kcal/mol simulation the $P(J)$ distribution for all of the trajectories is fit by a single Boltzmann at the surface temperature, which corresponds to an average rotational energy of $RT = 0.60$ kcal/mol. The difference between this rotational energy and the total rotational energy of 0.90 kcal/mol, listed in Table 5, is approximately the 0.28 kcal/mol associated with the vibrational angular momentum.

E. Scattering Angle Distributions. Figure 10 gives, for each collision energy, the scattering angle distribution $P(\theta)$, with θ defined as the angle between the initial and final CO₂ velocity vectors. The former is parallel to the surface normal. The solid line in the figure is the distribution $\sin \theta \cos \theta$ for random scattering.²² If the scattering is collected in only one plane, this random $P(\theta)$ is $\cos \theta$.⁵⁶ Listed in Table 8, for each E_i , is the

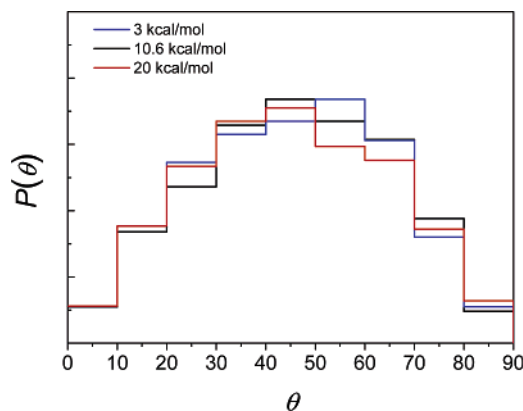


Figure 10. Distribution of the scattering angle (final CO₂ velocity with respect to the surface normal) for each collision energy. Properties of the distributions are listed in Table 8.

TABLE 8: Average Scattering Angles for Different Trajectory Types^a

E_i	average scattering angle $\langle \theta \rangle$			
	direct	penetrate	physisorb	total
3.0	36.6	44.5	49.1	45.3
10.6	35.6	44.1	54.7	45.8
20.0	34.2	42.4	58.5	44.9

^a Energy is in kcal/mol and angles are in degrees.

average scattering angle $\langle \theta \rangle$, for the total trajectories and each trajectory type.

The $P(\theta)$ are well-approximated by $\sin \theta \cos \theta$ for random scattering, with the highest energy $P(\theta)$ in the best agreement with this model. As shown in Table 8, the $\langle \theta \rangle$ values for the total trajectory $P(\theta)$ are all nearly equal to the value of 45° for random scattering. Table 8 also shows that the $\langle \theta \rangle$ values are not the same for the different trajectory types and that there is substantial averaging of these values to give $\langle \theta \rangle \sim 45^\circ$ for the total trajectories. The value of $\langle \theta \rangle$ is approximately 45° for the penetrating trajectories and smaller and larger than this value for the direct and physisorption trajectories, respectively. Overall, the total $P(\theta)$ distribution for normal incidence provides very little information concerning the different types of trajectories and their scattering dynamics. $P(\theta)$ may provide more information for nonnormal incident collisions.

IV. Comparison with Experiments

Nesbitt and co-workers have measured properties associated with the dynamics of CO₂ scattering off PFPE at $E_i = 10.6$ kcal/mol, $\theta_i = 0^\circ$, and with a surface temperature of 298 K.³¹ These collision conditions are considered for the study reported here of CO₂ + F-SAM scattering. Though there are differences in these two scattering systems, e.g., the PFPE structure is substantially more heterogeneous than that of the F-SAM, they have important similarities. The CO₂-surface intermolecular potential is similar for the PFPE and F-SAM surfaces, both the intermolecular and intramolecular potentials are similar for the two surfaces, and the surfaces have similar atomic constituents, leading to similar mass relationships for CO₂-surface collisions. Thus, it is of interest to compare the CO₂ + PFPE and CO₂ + F-SAM scattering dynamics.

The two quantities determined in the experiments³¹ are the rotational quantum number distribution $P(J)$ of the scattered CO₂ molecules and the Doppler widths of the laser absorption profiles, parallel to the surface. The latter are determined versus J and give the translational temperature of the scattered CO₂

for motion parallel to the surface. Significantly more trajectories are required than reported here to determine statistically meaningful Doppler profiles versus J . This work is in progress,⁵⁷ along with additional simulations to compare with the CO₂ + PFPE scattering. However, a comparison may be made between the CO₂ + PFPE and CO₂ + F-SAM $P(J)$ distributions.

As found here for the CO₂ + F-SAM system, the $P(J)$ distributions for CO₂ + PFPE collisions at $E_i = 10.6$ kcal/mol and $\theta_i = 0^\circ$ may also be fit by a sum of two Boltzmann distributions.³¹ The low-temperature component, set to 298 K, comprises $54 \pm 3\%$ of the distribution. The remainder of the distribution consists of the high-temperature component whose temperature was varied and found to be 715 ± 36 K. This $P(J)$ distribution is in remarkable good agreement with the one found here for CO₂ + F-SAM scattering for the same collision conditions. The percentages of its low- and high-temperature components, as given in Table 7, are 58 and 42, respectively, and their temperatures are 292 and 765 K. In the determination of these fractions and temperatures, the low temperature was allowed to vary and not fixed at the 300 K surface temperature for the simulations. If this temperature is fixed, as done in fitting the experimental CO₂ + PFPE $P(J)$ distribution, the respective low and high temperatures and fractions are 300, 0.60 and 786, 0.40.

The good agreement between the simulated and experimental $P(J)$ distributions indicates that CO₂ scattering is similar for collisions with the PFPE and F-SAM surfaces and that the trajectories accurately represent the scattering dynamics. Confirmation of this suggestion will require additional comparisons with experiment and simulations of CO₂ + PFPE scattering.⁵⁷

V. Discussion

A. Scattering Events. Three different types of trajectories were identified in the simulations: (1) direct CO₂ scattering from the top of the F-SAM surface, with only one inner turning point in the CO₂ motion perpendicular to the surface plane; (2) CO₂ physisorption on the top of the surface; and (3) CO₂ penetration of the surface. The latter is identified by an atom of CO₂ entering the SAM deeper than a height midway between that of the carbon atoms of the terminal $-\text{CF}_3$ groups and their adjacent $-\text{CF}_2$ groups. This is a phenomenological approach for identifying collision events, and other approaches have been used.^{22,27} However, this approach distinguishes between direct events and those that interact more strongly with the surface, including penetration.

As shown in Table 3, there is a slight decrease in the fraction of physisorption trajectories with an increase in E_i . In comparison, there is a significant increase and decrease in the direct and penetrating trajectories, respectively, as E_i is increased from 3.0 kcal/mol to the higher values. This decrease in the penetrating trajectories is somewhat unexpected, since more penetration of the surface might be expected for the higher E_i . The implication, from the observed result, is that a substantial fraction of the penetrating trajectories at $E_i = 3.0$ kcal/mol are preceded by physisorption, and an analysis of the trajectories shows that this indeed is the case. At $E_i = 3.0$ kcal/mol, 38% of the trajectories penetrate the surface, and of this percentage, 7% penetrate directly, whereas 31% penetrate following physisorption. Thus, 81% of the penetration is preceded by physisorption. For the higher E_i of 10.6 kcal/mol, 63% of the penetration occurs by physisorption penetration. This type of penetration comprises only 36% of the total penetration at $E_i = 20.0$ kcal/mol. Thus, direct penetration becomes a higher fraction of the penetration as E_i is increased.

With the above identification of two types of penetrating trajectories, the respective percentages of the direct, direct penetration, physisorption penetration, and physisorption trajectories are as follows: $E_i = 3.00$ kcal/mol with 17, 7, 31, and 45%; $E_i = 10.6$ kcal/mol with 34, 9, 15, and 42%; and $E_i = 20$ kcal/mol with 39, 16, 9, and 36%. The percentage of the trajectories which involve physisorption decreases with the values of 76, 57, and 45% as E_i is increased to 3.00, 10.6, and 20.0 kcal/mol.

B. Comparison of the $P(E_f)$ and $P(J)$ Distributions.

Following previous work,^{4,23,50,51} the distribution of the scattered CO₂ translational energy, $P(E_f)$, was deconvoluted into a Boltzmann component, with a fitted fraction and temperature, and a remaining high energy non-Boltzmann component. This deconvolution was possible for the penetrating, physisorption, and total trajectories but not for the direct trajectories. The latter do not contain a Boltzmann component. As shown in Table 6, the Boltzmann component comprises nearly all of $P(E_f)$ for the penetrating trajectories at all of the E_i (i.e., the Boltzmann fraction varies from 0.91 to 1.00), with thermal accommodation at the two lowest E_i and near accommodation at the highest E_i . A substantially different result is found for the physisorption trajectories. For E_i of 3.0 kcal/mol, all of $P(E_f)$ is fit by a Boltzmann distribution with a temperature of 364 K, i.e., only slightly larger than the surface temperature. However, for the higher E_i the Boltzmann component is 0.6–0.7, and its temperature is significantly higher than the surface temperature, e.g., 617 K for $E_i = 20.0$ kcal/mol.

A fundamental difference between the Boltzmann fits to the $P(J)$ and $P(E_f)$ distributions is that $P(J)$ may be fit by a sum of two Boltzmanns, whereas $P(E_f)$ is fit by a single Boltzmann and a remaining high energy, non-Boltzmann component. Nevertheless, given this difference, in the following the Boltzmann component in $P(E_f)$ is compared with the low-temperature component in $P(J)$ for the penetrating and physisorption trajectories (see Table 7). For an E_i of 3.0 and 10.6 kcal/mol, $P(J)$ for the penetrating trajectories is fit by a single Boltzmann with a temperature within 5 K of the surface temperature, and nearly the same is found for $P(E_f)$. Thus, for these E_i the $P(J)$ and $P(E_f)$ distributions have very similar properties. For the highest E_i of 20.0 kcal/mol, there are significant differences between the $P(E_f)$ and $P(J)$ distributions for the unconstrained fit to $P(J)$. However, as discussed in Section III.C, constraining the low-temperature component of $P(J)$ to 300 K may be more realistic. This gives a 300 K component comprising 94% of $P(J)$, which agrees with $P(E_f)$, whose Boltzmann component at 340 K comprises 91% of the distribution.

At $E_i = 3.0$ kcal/mol the $P(E_f)$ and $P(J)$ distributions for the physisorption trajectories are both fit by a single Boltzmann, with respective temperatures of 364 and 304 K. For the physisorption trajectories at the higher E_i , the fraction of the low-temperature component in $P(J)$ is similar to the fraction of the Boltzmann component in $P(E_f)$. However, the temperatures for these two components are not the same. For example, at $E_i = 20.0$ kcal/mol the low temperature is 357 K in the fit to $P(J)$, whereas the temperature of the Boltzmann component in $P(E_f)$ is 617 K. Overall, $P(E_f)$ and $P(J)$ for the physisorption trajectories have similar properties at 3.0 kcal/mol but not at the higher E_i where nonaccommodated dynamics is important.

C. Identifying Trapping Desorption and Inelastic Scattering Events. In analyses of experimental studies of gas–surface scattering,^{50,51} $P(E_f)$ is often deconvoluted into a Boltzmann component and a remaining non-Boltzmann component consisting of trajectories with higher translational

energies. It is customary to identify the Boltzmann component as trapping desorption (TD) and the high energy component as inelastic scattering (IS). It is of interest to compare this model with the CO₂ + F-SAM atomic-level dynamics reported here.

For the $E_i = 3.0$ kcal/mol simulations, $P(E_f)$ for the total trajectories is fit by a single Boltzmann with a temperature of 365 K, which is only slightly higher than the surface temperature of 300 K. Similarly, the $P(J)$ distribution for the total trajectories is also fit by a single Boltzmann but with a temperature of 302 K that is essentially the same as that of the surface. The ability to fit both $P(E_f)$ and $P(J)$ by a single Boltzmann distribution, with a temperature nearly the same as the surface, would be identified as 100% TD by the standard analysis. However, as shown in Table 3, 17% of the trajectories are direct events with neither penetration nor physisorption.

For the $E_i = 10.6$ kcal/mol simulations, 34% of the trajectories gave direct CO₂ + F-SAM scattering, and 24% and 42% penetrated and physisorbed, respectively. The $P(E_f)$ distribution for the total trajectories has a Boltzmann component at 360 K, which comprises 63% of the distribution. This percentage is similar to the total percentage of penetrating and physisorbing trajectories, i.e., 64%. The $P(J)$ distribution has a low-temperature component at 292 K, which comprises 58% of the distribution, which is also close to the combined percentage of penetrating and physisorbing trajectories. Thus, for the $E_i = 10.6$ kcal/mol simulations, the deconvolution of either the $P(E_f)$ or $P(J)$ distribution yields a Boltzmann component, with a temperature near that of the surface and whose fraction is nearly equal to the sum of the fractions of the penetrating and physisorbing trajectories. However, this deconvolution does not identify the finding that the penetrating trajectories thermally accommodate whereas the physisorbing ones do not.

In contrast to the above findings for the two lowest E_i , at E_i of 20.0 kcal/mol the amount of TD suggested by deconvoluting the total trajectory $P(E_f)$ and $P(J)$ distributions is inconsistent (see Tables 6 and 7) and disagrees with the fractions of the actual trajectory types (see Table 3).

D. Importance of Penetration for Collisions with H-SAM and F-SAM Surfaces. An interesting dynamical feature of the CO₂ + F-SAM collisions is the importance of surface penetration. This mechanism is enhanced by physisorption, and the probability of penetration decreases from 38% of the trajectories to 25% as E_i is increased from 3.0 to 20.0 kcal/mol. Though there are no previous studies of small projectiles scattering off F-SAM surfaces, these results may be compared with studies of H-SAM scattering.^{10,17,26} The probability of Ar-atom penetration of the H-SAM has been studied using model surface structures with different spacings between the alkanethiol chains.¹⁰ For a collision angle of 30° and energies of 14.3 and 19.1 kcal/mol, penetration is negligible for the experimental chain spacing of 4.98 Å but comprises 23% of the trajectories for both of these collision energies when the spacing is increased to 5.40 Å.

Penetration of the H-SAM is important for O-atom scattering at a collision angle of 15°,¹⁷ similar to that of a 0° collision angle for CO₂ + F-SAM scattering. O-atom collisions at energies of 0.12, 2.3, and 11.2 kcal/mol give 12, 27, and 53% penetration, respectively. At the lowest E_i of 0.12 kcal/mol penetration is preceded by physisorption, but for the higher E_i direct penetration becomes important. For CO₂ + F-SAM scattering direct penetration also increases with an increase in E_i , constituting 7, 9, and 16% of the trajectories for E_i of 3.0, 10.6, and 20.0 kcal/mol, whereas physisorption penetration decreases with values of 31, 15, and 9%.

Overall, O + H-SAM inelastic scattering is very similar to that for Ne + H-SAM collisions.¹⁷ However, no surface penetration was observed in a simulation of Ne + H-SAM collisions in which only specular scattering was analyzed.²⁶ The H-SAM experiment temperature was at 135 K in this study as compared to 300 K for the above studies. Both of these attributes of the simulation diminish the probability of penetration. The colder surface results in fewer fluctuations of the surface structure, providing “openings” for surface penetration. Specular scattering favors direct events over more long-lived surface events, such as penetration, which tend to scatter more randomly. A careful comparison of surface penetration in the O + H-SAM and Ne + H-SAM studies indicates their different probabilities for penetration arise from differences in the simulations’ initial conditions, constraints for trajectory analyses, and details of the simulation models.¹⁷

It is important to characterize the atomic-level mechanisms for gas–surface scattering, and it is expected that additional comparisons such as those given above will be made in the future. Comparisons of the same projectile scattering off different surfaces or of different projectiles scattering off the same surface are both of substantial interest.

VI. Summary

In the work presented here chemical dynamics simulations were used to study scattering of CO₂ off a F-SAM surface. The potential energy function for the F-SAM was developed from previous work,³² and the CO₂ + F-SAM intermolecular potential was developed from high level ab initio calculations. Perpendicular collisions with the surface at energies of 3.0, 10.6, and 20.0 kcal/mol were investigated. The following attributes of the scattering dynamics were determined from this study:

(1) The atomic-level mechanism for the scattering consists of three trajectory types, direct scattering, penetration of the F-SAM, and physisorption of the F-SAM. The latter two events are followed by desorption. The direct scattering and physisorption probabilities increase and decrease, respectively, with an increase in E_i . There are two types of penetration events, direct penetration and physisorption penetration. For the former the trajectories directly enter the F-SAM, whereas they first physisorb for the latter. With an increase in E_i , direct penetration increases and physisorption penetration decreases.

(2) Most of the incident energy goes to the surface’s vibrational modes, with this transfer increasing from 34 to 73% as E_i is increased from 3.0 to 20.0 kcal/mol. Concomitantly, the percentage remaining in CO₂ translation and in the CO₂ internal degrees of freedom decreases. The latter is 19, 9, and 7% at E_i of 3.0, 10.6, and 20.0 kcal/mol, respectively. This transfer is primarily attributed to CO₂ rotation.

(3) The relative translational energy and rotational angular momentum distributions, $P(E_f)$ and $P(J)$, were analyzed for each trajectory type of the scattered CO₂ molecules. There is efficient thermal accommodation for the penetrating trajectories, and their $P(E_f)$ and $P(J)$ distributions are similar at each E_i . Each distribution has an ~300 K Boltzmann component whose fraction comprises 0.9–1.0 of the distribution. At $E_i = 3.0$ kcal/mol, $P(E_f)$ and $P(J)$ are similar for the physisorption trajectories, each consisting of a single Boltzmann approximately at the surface temperature. However, at the higher E_i the forms of these two distributions are different. This is consistent with the absence of thermal accommodation for the physisorption trajectories at the higher E_i . The direct scattering trajectories have an approximately single Boltzmann $P(J)$ distribution at the surface temperature for E_i of 3.0 kcal/mol, but the $P(E_f)$

distribution is non-Boltzmann for all the E_i . Thus, at each collision energy, the forms of $P(E_f)$ and $P(J)$ are different for the direct trajectories.

(4) The $P(J)$ distribution for the scattered CO₂ molecules, in the CO₂ + F-SAM simulation, is nearly identical to that measured for CO₂ scattering off a PFPE surface.³¹ $P(J)$ for CO₂ + F-SAM scattering is fit by a sum of two Boltzmann distributions, with one at the surface temperature, which comprises 58% of the distribution. In contrast, for the experimental study of CO₂ + PFPE scattering, 54% of $P(J)$ consists of this Boltzmann component. This agreement suggests that the dynamics are similar for CO₂ molecules scattering off F-SAM and PFPE surfaces, which is a very interesting result that should be investigated by future experimental and computational studies.

Finally, it is important to emphasize that the current simulation only addresses perpendicular CO₂ collisions with the F-SAM surface compared with experiments.³¹ For more glancing collisions the relative importance of the different trajectory types may vary; e.g., penetration may be less important, and there may be less energy transfer. Such effects were observed in simulations of O(³P) + H-SAM scattering.¹⁷

Acknowledgment. E.M.N. would like to thank the “Ministerio de Ciencia y Tecnología” (Spain) for the financial support received through the “Ramón y Cajal” program. This material is also based upon work at Texas Tech University supported by the Air Force Office of Scientific Research, the Robert A. Welch Foundation under Grant No. D-0005, and the National Science Foundation under Grant No. 0412677. The authors wish to acknowledge important discussions with David Nesbitt and Bradford Perkins, Jr.

References and Notes

- (1) Cohen, S. R.; Naaman, R.; Sagiv, J. *Phys. Rev. Lett.* **1987**, *58*, 1208.
- (2) Tully, J. C. *J. Chem. Phys.* **1990**, *92*, 680.
- (3) Saecker, M. E.; Govoni, S. T.; Kowalski, D. V.; King, M. E.; Nathanson, G. M. *Science* **1991**, *252*, 1421.
- (4) Bosio, S. B. M.; Hase, W. L. *J. Chem. Phys.* **1997**, *107*, 9677.
- (5) Garton, D. J.; Minton, T. K.; Alagia, M.; Balucani, N.; Casavecchia, P.; Volpi, G. G. *Faraday Discuss.* **1998**, *108*, 3871.
- (6) Shuler, S. S.; Davis, G. M.; Morris, J. R. *J. Chem. Phys.* **2002**, *116*, 9147.
- (7) Gibson, K. D.; Isa, N.; Sibener, S. J. *J. Chem. Phys.* **2003**, *119*, 13083.
- (8) Day, B. S.; Morris, J. R.; Troya, D. *J. Chem. Phys.* **2005**, *122*, 214712.
- (9) Day, B. S.; Morris, J. R. *J. Chem. Phys.* **2005**, *122*, 234714.
- (10) Day, B. S.; Morris, J. R.; Alexander, W. A.; Troya, D. *J. Phys. Chem. A* **2006**, *110*, 1319.
- (11) Gibson, K. D.; Isa, N.; Sibener, S. T. *J. Phys. Chem. A* **2006**, *110*, 1469.
- (12) Li, G.; Bosio, S. B. M.; Hase, W. L. *J. Mol. Struct.* **2000**, *556*, 43.
- (13) Zhang, J.; Garton, D. J.; Minton, T. K. *J. Chem. Phys.* **2002**, *117*, 6239.
- (14) Troya, D.; Schatz, G. C. *J. Chem. Phys.* **2004**, *120*, 7696.
- (15) Köhler, S. P. K.; Allan, M.; Kelso, H.; Henderson, D. A.; McKendrick, K. G. *J. Chem. Phys.* **2005**, *122*, 024712.
- (16) Köhler, S. P. K.; Allan, M.; Costen, M. L.; McKendrick, K. G. *J. Phys. Chem. B* **2006**, *110*, 2771.
- (17) Tasić, U. S.; Yan, T.; Hase, W. L. *J. Phys. Chem. B* **2006**, *110*, 11863.
- (18) Day, B. S.; Shuler, S. F.; Ducre, A.; Morris, J. R. *J. Chem. Phys.* **2003**, *119*, 8084.
- (19) Ferguson, M. K.; Lohr, J. R.; Day, B. S.; Morris, J. R. *Phys. Rev. Lett.* **2004**, *92*, 073201.
- (20) Day, B. S.; Morris, J. R. *J. Phys. Chem. B* **2003**, *107*, 7120.
- (21) Morris, J. R. Private communication.
- (22) Yan, T.; Hase, W. L. *Phys. Chem. Chem. Phys.* **2000**, *2*, 901.
- (23) Yan, T.; Hase, W. L.; Barker, J. R. *Chem. Phys. Lett.* **2000**, *329*, 84.
- (24) Yan, T.; Hase, W. L. *J. Phys. Chem. A* **2001**, *105*, 2617.
- (25) Yan, T.; Hase, W. L. *J. Phys. Chem. B* **2002**, *106*, 8029.
- (26) Yan, T.; Isa, N.; Gibson, K. D.; Sibener, S. J.; Hase, W. L. *J. Phys. Chem. A* **2003**, *107*, 10600.
- (27) Isa, N.; Gibson, K. D.; Yan, T.; Hase, W. L.; Sibener, S. J. *J. Chem. Phys.* **2004**, *120*, 2417.
- (28) Gibson, K. D.; Isa, N.; Sibener, S. J. *J. Chem. Phys.* **2003**, *119*, 13083.
- (29) Lohr, J. R.; Day, B. S.; Morris, J. R. *J. Phys. Chem. B* **2005**, *109*, 15469.
- (30) Lohr, J. R.; Day, B. S.; Morris, J. R. *J. Phys. Chem. A* **2006**, *110*, 1645.
- (31) Perkins, B. G., Jr.; Häber, T.; Nesbitt, D. J. *J. Phys. Chem. B* **2005**, *109*, 16396.
- (32) Borodin, O.; Smith, G. D.; Bedrov, D. *J. Phys. Chem. B* **2002**, *106*, 9912.
- (33) (a) Davies, P. R.; Orville-Thomas, W. J. *J. Mol. Struct.* **1969**, *4*, 163. (b) Person, W. B.; Zerbi, G. *Vibrational Intensities in Infrared and Raman Spectroscopy*; Elsevier: Amsterdam, 1982. (c) Shimanouchi, T. *Tables of Molecular Vibrational Frequencies, Consolidated Volume 1*; NSRDS NBS-39, U.S. Department of Commerce: Washington, DC, 1972.
- (34) Liu, G.-y.; Fenter, P.; Chidsey, C. E. D.; Ogletree, D. F.; Eisenberger, P.; Salmeron, M. *J. Chem. Phys.* **1994**, *101*, 4301.
- (35) Sellers, H.; Ulman, A.; Shnidman, Y.; Eilers, J. E. *J. Am. Chem. Soc.* **1993**, *115*, 9389.
- (36) Möller, C.; Plesset, M. S. *Phys. Rev.* **1934**, *46*, 618.
- (37) Dunning, T. H., Jr. *J. Chem. Phys.* **1989**, *90*, 1007.
- (38) Boys, S. B.; Bernardi, F. *Mol. Phys.* **1970**, *19*, 553.
- (39) Peterson, K. A.; Woon, D. E.; Dunning, T. H., Jr. *J. Chem. Phys.* **1994**, *100*, 7410.
- (40) The program for the nonlinear least-squares fitting is a modification of the Levenberg–Marquardt algorithm and was taken from the Netlib Repository. www.netlib.org.
- (41) Diep, P.; Jordan, K. D.; Johnson, J. K.; Beckman, E. J. *J. Phys. Chem. A* **1998**, *102*, 2231.
- (42) Fried, J. R.; Hu, N. *Polymer* **2003**, *44*, 4363.
- (43) Tasić, U. S.; Alexeev, Y.; Vayner, G.; Crawford, D.; Windus, T. L.; Hase, W. L. *Phys. Chem. Chem. Phys.*, in press.
- (44) East, A. L. L.; Allen, W. D. *J. Chem. Phys.* **1993**, *99*, 4638.
- (45) Alexander, W. A.; Troya, D. *J. Phys. Chem. A* **2006**, *110*, 10834.
- (46) VENUS05 is an enhanced version of VENUS96, with additional algorithms. VENUS96 is available on the website cdssim.chem.ttu.edu and was initially released through the Quantum Chemistry Program Exchange (QCPE) Bulletin **1996**, *16*, 671.
- (47) Peshlherbe, G. H.; Wang, H.; Hase, W. L. In *Monte Carlo Methods in Chemical Physics, Advances in Chemical Physics*; Ferguson, D. M., Siepmann, J. I., Truhlar, D. G., Eds.; Wiley: New York, 1999; Vol. 105, pp 171–201.
- (48) Allen, M. P.; Tildesley, D. J. *Computer Simulation of Liquids*; Oxford: New York, 1987.
- (49) See the URL <http://monte.chem.ttu.edu>.
- (50) Saecker, M. E.; Nathanson, G. M. *J. Chem. Phys.* **1993**, *99*, 7056.
- (51) Nathanson, G. M. *Annu. Rev. Phys. Chem.* **2004**, *55*, 231.
- (52) Levine, I. N. *Molecular Spectroscopy*; Wiley: New York, 1975; pp 271–277.
- (53) Califano, S. *Vibrational States*; Wiley: New York, 1976; pp 37–41.
- (54) Aoiz, F. J.; Banares, L. J. *J. Phys. Chem.* **1996**, *100*, 18108.
- (55) Grimmelmann, E. K.; Tully, J. C.; Cardillo, M. J. *J. Chem. Phys.* **1980**, *72*, 1039.
- (56) Goodman, F. O.; Wachman, H. Y. *Dynamics of Gas–Surface Scattering*; Academic: New York, 1976.
- (57) Martínez-Núñez, E.; Rahaman, A.; Perkins, B. G., Jr.; Nesbitt, D. J.; Hase, W. L. Work in progress.